Responses of GNSS ZTD Variations to ENSO Events and Prediction Model Based on FFT-LSTME

Tengli Yu, Ershen Wang, Shuanggen Jin, *Senior Member, IEEE*, Yong Wang,
Jing Huang, Xiao Liu, and Wei Zhan

***Abstract*— The El Niño-Southern Oscillation (ENSO) event often causes natural disasters in mainland China. Existing quantitative analysis of ENSO event's effects on climate change in mainland China is insufficient. The monthly scale prediction effectiveness of ENSO events is still low. Global Navigation Satellite System (GNSS) can estimate zenith tropospheric delay (ZTD) with high accuracy, which can study ZTD responses to ENSO and improve the prediction accuracy of ENSO events. This study quantitatively analyzed the response patterns of GNSS ZTD time–frequency variation to ENSO events in mainland China. The monthly multivariate ENSO index (MEI) thresholds for GNSS ZTD anomaly response to ENSO events are (−1.12, 1.92) for the tropical monsoon zone (TPMZ), (−1.12, 1.61) for the subtropical monsoon zone (SMZ), (−1.19, 1.62) for the temperate monsoon zone (TMZ), (−1.26, 1.64) for the temperate continental zone (TCZ), and (−1.22, 1.72) for the mountain plateau zone (MPZ). The ENSO event causes the amplitude of the nine-month variation period to decrease and the amplitude of the 0.8–3-month period to increase for the GNSS ZTD in mainland China. Furthermore, a forecasting model is proposed by integrating fast Fourier transform and long short-term memory extended (FFT-LSTME). The model uses monthly MEI as the primary input and the GNSS ZTD reconstruction sequence that responds to ENSO as the auxiliary input. It can predict ENSO events in the next 24 months with an index of agreement (IA) of 91.56% and a root mean square error (RMSE) of 0.25. The RMSE is optimized by 70.48%, 43.95%, and 11.6% when compared with radial basis function (RBF), LSTM, and FFT-LSTM.**

***Index Terms*— El Niño-Southern Oscillation (ENSO), Global Navigation Satellite System (GNSS) meteorology, long short-term memory extended (LSTME), zenith tropospheric delay (ZTD).**

I. INTRODUCTION

IN RECENT years, the frequency of extreme weather and climate events in mainland China has been increasing, causing severe harm to human production and life. For example, the heavy rain event that occurred in July 2021 affected a wide range of jurisdictions in Henan Province, China, resulting in significant economic losses and social impacts. The National Climate Center of China Meteorological Administration indicates that this event is related to La Niña (the cold phase event of the El Niño-Southern Oscillation (ENSO) event). The Global Navigation Satellite System (GNSS) meteorological elements are also a good indicator of this catastrophic rainstorm event [1]. Global extreme weather monitoring and early warning capability are improving, and disaster prevention and mitigation effectiveness have been significantly enhanced. Against the background of increasing global warming, the climate system is, however, actively changing, and the formation mechanism of ENSO events is complex and difficult to predict precisely. ENSO events indirectly cause catastrophic effects on China's climate by affecting precipitable water vapor (PWV) transport in the East Asian monsoon region [2]. The monitoring and early warning accuracy of ENSO events need to be further improved to ensure the health and property safety of the people. Applying GNSS meteorology to monitoring and early warning of ENSO events is a new prospective method, and it can provide technical references for relevant meteorological departments.

GNSS technology has the advantages of continuous operation, high accuracy, and low cost [3], [4], [5]. Remote sensing of the troposphere using GNSS to obtain relevant meteorological data, called "GNSS meteorology," is an essential technique for monitoring climate change [6], [7], [8]. The standard product of GNSS meteorology is the zenith tropospheric delay (ZTD). The GNSS signal is influenced by the refraction effect of the atmospheric medium when passing through the troposphere, thus causing a delay in signal transmission. The resulting path delay is called ZTD [9]. GNSS ZTD

Manuscript received 18 September 2022; revised 17 January 2023; accepted 21 February 2023. Date of publication 2 March 2023; date of current version 16 March 2023. This work was supported in part by the National Natural Science Foundation of China under Grant 62173237; in part by the SongShan Laboratory Foundation under Grant YYJC062022017; in part by the Open Fund of Key Laboratory of Civil Aviation Flights Wide Area Surveillance and Safety Control Technology, Civil Aviation University of China, under Grant 202105; in part by the Applied Basic Research Programs of Liaoning Province under Grant 2022020502-JH2/1013; in part by the Open Fund of Key Laboratory of Flight Techniques and Flight Safety Civil Aviation Administration Of China (CAAC) under Grant FZ2021KF15 and Grant FZ2021ZZ06; in part by the Special Funds Program of Civil Aircraft under Grant 01020220627066; in part by the Special Funds Program of Shenyang Science and Technology under Grant 22-322-3-34; and in part by State Key Laboratory of Geodesy and Earth's Dynamics, Innovation Academy for Precision Measurement Science and Technology (IPM), Chinese Academy of Sciences (CAS) under Grant SKLGED-2021-2-4. *(Corresponding authors: Yong Wang; Ershen Wang.)*

Tengli Yu is with the School of Aerospace Engineering, Shenyang Aerospace University, Shenyang 110136, China (e-mail: yutengli97@163.com).

Ershen Wang is with the School of Electronic and Information Engineering and the Liaoning General Aviation Academy, Shenyang Aerospace University, Shenyang 110136, China (e-mail: wes2016@sau.edu.cn).

Shuanggen Jin is with the School of Surveying and Land Information Engineering, Henan Polytechnic University, Jiaozuo 454000, China, and also with the Shanghai Astronomical Observatory, Chinese Academy of Sciences, Shanghai 200030, China (e-mail: sgjin@shao.ac.cn).

Yong Wang is with the School of Geology and Geomatics, Tianjin Chengjian University, Tianjin 300384, China, and also with the State Key Laboratory of Geodesy and Earth's Dynamics, Chinese Academy of Sciences (CAS), Wuhan 430077, China (e-mail: wangyongjz@126.com).

Jing Huang is with the School of Geology and Geomatics, Tianjin Chengjian University, Tianjin 300384, China.

Xiao Liu and Wei Zhan are with the First Monitoring and Application Center, China Earthquake Administration, Tianjin 300180, China.

Digital Object Identifier 10.1109/TGRS.2023.3251375

has fewer sources of error because it avoids the subsequent inversion process [10]. Researchers found that GNSS ZTD has a strong correlation with extreme climate events and evaluated the application value of GNSS ZTD in identifying climate events such as heavy rainfall, drought, and heavy haze weather [10], [11], [12], [13], [14]. GNSS ZTD is widely used in numerical weather forecasts and extreme climate monitoring [15], [16], [17], [18].

ENSO events have global impacts on ecosystems, manifesting as La Niña events in the cold phase and El Niño events in the warm phase [19]. Researchers refer to El Niño events with the sea surface temperature (SST) anomaly warming region in the central equatorial Pacific as Central-Pacific types of El Niño (CP-El Niño) and El Niño events with the SST anomaly warming region in the eastern tropical Pacific as Eastern-Pacific types of El Niño (EP-El Niño) [20]. This criterion also distinguishes La Niña events. Related scholars have analyzed the impact of ENSO events on the climate change in mainland China using precipitation, temperature, and other meteorological elements. The results show that the response characteristics of climate change in different regions of mainland China to different types of ENSO events differ [21], [22]. Foster et al. [23] first explored the impact of ENSO events on climate change using GNSS stations in tropical monsoon climate zones. Barindelli et al. [24] and Zhao et al. [25] also successively demonstrated the correlation between different types of ENSO events and meteorological elements using GNSS observations. Yao et al. [26] demonstrated the existence of a significant semiannual period of GNSS ZTD and the response of the abnormal variation of this cycle to El Niño events. Wang et al. [27] studied the influence of El Niño events on climate changes in mainland China using the Chinese regional GNSS ZTD. The above studies show that GNSS ZTD can indicate the evolution of ENSO events, which provides theoretical support for applying GNSS meteorology to ENSO event prediction. There are differences in the selection of individual cases in the above studies, so the results of the studies are, however, not the same, and there is a lack of quantitative analysis to explore the exact threshold of the impact of ENSO events on climate change in the Chinese region. Therefore, this study will systematically quantify the response patterns of different regions' climate change in mainland China to different ENSO events.

Currently, the forecasting methods for ENSO events mainly include numerical and statistical forecasting models. Numerical prediction models have complex structures, are computationally intensive, and require cumbersome computer resource configurations [28]. Ren et al. said that due to the complex nonlinear evolution characteristics of ENSO, the current climate numerical prediction model still has significant errors in reproducing the diversity and complexity of ENSO. It is urgent to improve and upgrade the model and fully use new techniques, such as neural networks, to correct the model output [29]. Statistical forecasting models use historical time series data to predict future data. Statistical models are less computationally intensive, have low system operation costs, and have higher accuracy of forecast results. Statistical models commonly include machine learning (ML) and artificial neural network (ANN) models. The ML model has a clear mathematical logic and a simple structure; however, these models can easily be overfitted if the parameters are not set properly. With the development of artificial intelligence, ANN models, especially deep learning models, have features such as nonlinear mapping, adaptive mapping, and robustness [30], which provide better performance in nonlinear prediction tasks. Radial basis function (RBF), recurrent neural network (RNN), convolutional neural network (CNN), and long short-term memory (LSTM) neural network are the more commonly used neural network models. Ham et al. [31] constructed an ENSO event prediction model based on CNN, which can predict the occurrence of ENSO events up to 18 months in advance, and the accuracy can reach about 80%. This study fully demonstrates the feasibility of applying ANN methods in climate monitoring. This study, however, only used the Niño3.4 SST anomaly (SSTA) as a single variable for prediction, and the prediction accuracy needs to be improved. The RNN model applies to the processing of time series; however, for processing longer time series, RNN models are limited by problems such as gradient explosion or disappearance [32]. The LSTM model can effectively solve these problems and is suitable for predicting longer nonlinear time series. Related scholars have verified that LSTM models have significantly better prediction accuracy than traditional ML models such as support vector regression (SVR), multiple linear regression (MLR), decision tree regression (DTR), and random forest regression (RFR) [33], [34], [35]. LSTM models are widely used in the field of ENSO event prediction. Huang et al. [36] used SST as a predictor and verified that the traditional LSTM has better predictability than linear regression models. Chen [37] used the traditional LSTM model to predict the Southern Oscillation Index (SOI) with a root-mean-square error (RMSE) of 0.53 for a three-month prediction time horizon and 0.93 for a 12-month prediction time horizon. Zhou et al. [38] predicted the Niño3.4 index using a traditional LSTM with a 12-month prediction time horizon and an RMSE of 0.36. Guo et al. proposed a Niño3.4 index prediction model integrating empirical mode decomposition and LSTM and compared it with traditional LSTM, Autoregressive Integrated Moving Average (ARIMA), and SVR regression models. According to the results, the conventional LSTM performed better than ARIMA and SVR. The best prediction performance of the integrated empirical pattern decomposition and LSTM model was achieved with an RMSE of 0.3 at a 12-month prediction time [39]. Gupta et al. [40] proposed a convolutional LSTM network, which predicted the monthly value of the Niño3.4 index for the next 12 months with an average RMSE of 0.72 °C for 2009–2019.

The conventional LSTM models and various improved LSTM models in the above study carried out the prediction based only on the nonlinear characteristics of the ENSO event discriminant index itself, without adding other constraints. The Niño3.4 index or SOI is used as the primary predictor, and the prediction time limit is generally 6–12 months. The choice of predictors needs to be further explored. The prediction accuracy and timeliness of the model need to be further improved. Li et al. [41] effectively improved the prediction accuracy by adding auxiliary variables to the traditional LSTM model. Mao et al. [34] proposed an LSTM model with a time-sliding window to improve the prediction accuracy by using the optimal time lag of the prediction element itself as the window length. We have previously fused the fast Fourier transform with the traditional LSTM model (FFT-LSTM), which effectively improved the prediction accuracy of meteorological elements [42]. In this study, we will further optimize the FFT-LSTM neural network model and apply it to the prediction of ENSO events.

This study aims to construct an ENSO event prediction model incorporating high-precision GNSS ZTD to achieve longer timeliness and higher accuracy prediction. We selected an optimal ENSO event discriminant index [multivariate ENSO index (MEI)] as the predictor of ENSO events. Based on the spatial distribution characteristics of GNSS ZTD, the Chinese mainland was partitioned according to five major climate types. We analyzed and quantified the response of anomaly sequences and frequency domain oscillation features of GNSS ZTD in different regions to ENSO events. The time–frequency feature terms of the GNSS ZTD response to the presence of ENSO events were reconstructed and used as auxiliary inputs to the ENSO event prediction model. We proposed a prediction model based on LSTM extended network and FFT (FFT-LSTME). The function of FFT is to decrease the effect of temporal heterogeneity between GNSS ZTD and ENSO indices on the prediction effectiveness of the model. The optimal common variation period of GNSS ZTD and MEI is used as the model's input duration, and a time-sliding block is set within the LSTME neural network to achieve long-time prediction. Applying GNSS ZTD in the ENSO event monitoring and warning field can provide a reference for relevant meteorological monitoring and disaster prevention and control governance departments.

The remainder of the article is structured as follows. Section II introduces the datasets and study area division. Section III analyzes the response threshold of GNSS ZTD anomaly sequence to ENSO events from the time domain perspective. Section IV analyzes the response of GNSS ZTD frequency domain oscillation characteristics to ENSO events from the frequency domain perspective. Section V introduces the construction process and evaluation results of the ENSO event prediction model based on FFT-LSTME. Section VI is the discussion section of this article. Finally, the study is concluded in Section VII.

II. Data Processing and Study Area Division

A. CMTEMN ZTD

The ZTD in this study is provided by the First Monitoring and Application Center, China Earthquake Administration. The dataset was solved based on continuous GNSS observations from the China Mainland Tectonic Environment Monitoring Network (CMTEMN). CMTEMN is widely used in geodesy and climate monitoring [43], [44]. Its accuracy has been verified by researchers [45]. CMTEMN has 262 continuous stations, including 31 Chinese Crustal Movement Observation Network of China (CMONOC) stations (see Fig. 1). The data of the CMONOC reference stations have been recorded since 1999. The new 231 continuous stations of the CMTEMN have been producing data since mid-2010, and nearly 12 years of GNSS observations have been accumulated. The temporal resolution of ZTD (mm) and meteorological data are 1 h. Because of the different construction times of CMONOC and CMTEMN, the length of observation data accumulated at each site is different. We get the longest time series of GNSS ZTD: 2008/1–2021/6, and the shortest time series: 2011/1–2021/6. YONG, LALB, and LALX sites do not participate in the analysis due to the lack of data.

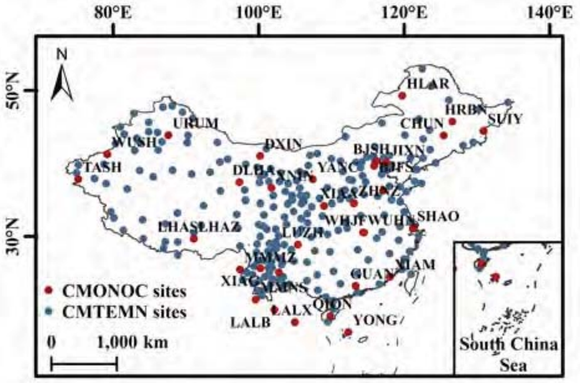

Fig. 1. GNSS sites distribution from CMONOC and CMTEMN.

B. GNSS ZTD Anomaly Sequences

According to the existing research, it can be seen that the change of the GNSS ZTD time series is mainly driven by significant change cycles and trend items such as the annual cycle, semi-annual cycle, and seasonal cycle [27]. The GNSS ZTD anomaly sequence can be obtained by removing the trend signal and the significant period signal [25]. Wavelet transform (WT) provides time domain localization corresponding to the frequency domain information of time series. It is widely used in signal processing, image processing, and many nonlinear scientific fields [46], [47], [48]. This article selects a compactly supported standard orthogonal Db6 wavelet basis function for the time–frequency analysis of the GNSS ZTD time series [49]. The layered principle of WT is used $2, 4, 8, \ldots, 2^J$ as the scale to decompose the signal $f(t)$ (frequency is $0 - F$) into $J + 1$ signal frequency bands. The frequency band $0 - F/2^J$ is the low-frequency term (AJ) and $F/2^n - F/2^{n-1} (n = 1, 2, 3, \ldots, J)$ is the high-frequency term (D1, D2, …, DJ). The corresponding period of each frequency band is shown in Table I. The criterion for stratification is that the AJ curve of the low-frequency signal exhibits a single increasing or decreasing trend. In this study, the WT decomposes the GNSS ZTD monthly-mean time series into seven layers. Then, the GNSS ZTD anomaly time series is obtained by separating the layers corresponding to the significant change period and trend term from them and reconstructing the remaining layers (see Fig. 2). The D1 layer corresponds to 2–4 monthly variation periods, D2 layer

TABLE I
CORRESPONDING PERIOD OF WAVELET COEFFICIENTS AT EACH SCALE

Layers	D1	D2	D3	D4	D5	D6	D7	A7
Period (month)	2–4	4–8	8–16	16–32	32–64	64–128	128–256	256–∞

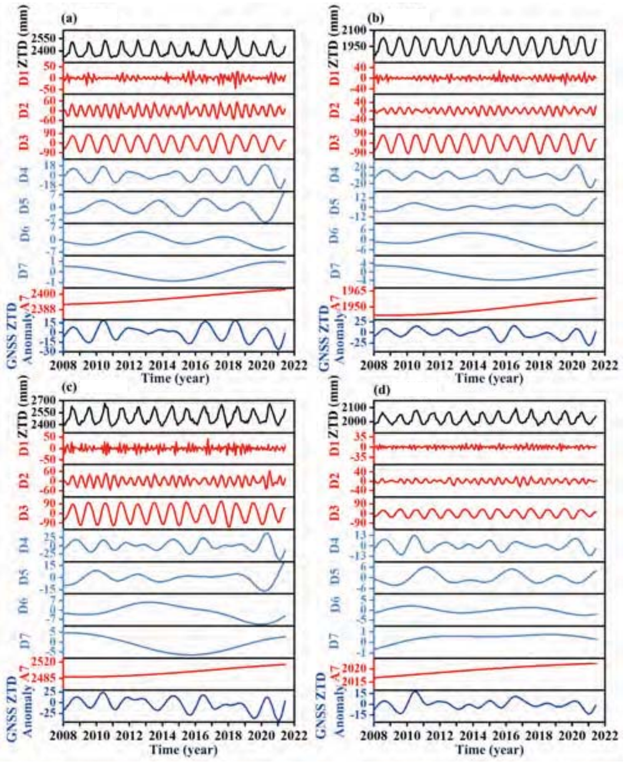

Fig. 2. GNSS ZTD time–frequency analysis and reconstruction. The black line is the original GNSS ZTD monthly mean sequence, the red line is the primary driver term of GNSS ZTD, and the dark blue line is the reconstructed GNSS ZTD anomaly sequence. (a) BJFS. (b) KMIN. (c) WUHN. (d) WUSH.

corresponds to the semi-annual period, D3 layer is the annual period, and A7 layer is the trend term. By comparing the amplitudes of wavelet coefficients at each scale, it can be found that the variation of GNSS ZTD is mainly driven by A7, D3, D2, and D1. Therefore, the GNSS ZTD anomaly sequence is obtained by removing D1, D2, D3, and A7 and reconstructing the high-frequency terms in layers D4–D7.

C. ENSO Event Discrimination

ENSO events consist of two components, El Niño (mainly for the ocean) and Southern Oscillation (mainly for the atmosphere). These two components are manifestations of the same phenomenon in different media, and the two phenomena form a cyclic system. With the continuous improvement of monitoring methods and monitoring areas, the discriminant index of ENSO events is also constantly developing. The SOI was most commonly used in the early days [50], which discriminated against ENSO events mainly from the atmospheric perspective. Later, Trenberth verified that using the SST Index in the Niño 3.4 region of the eastern Pacific was more accurate [51]. The National Oceanic and Atmospheric Administration (NOAA) defines the 3-month sliding average of the SSTA in Niño 3.4 as the Oceanic Niño index (ONI). Since the variation of Niño3.4 SSTA and SOI is sometimes not the same, Wolter and Timlin proposed an MEI. The index incorporates multiple atmospheric and oceanic meteorological elements to characterize ENSO events comprehensively [52]. A new version of the MEI (MEI.v2) has been created, which was obtained by principal component analysis of five variables: sea level pressure (SLP); SST; surface zonal winds (U), surface meridional winds (V), and outgoing longwave radiation (OLR) [53]. This study analyzed the three most commonly used ENSO event discriminating indices, SOI, ONI, and MEI, and selected the ones with the strongest correlation with GNSS ZTD in mainland China. The time of each index is from 2008 to the present, and the temporal resolution is one month (see Fig. 3).

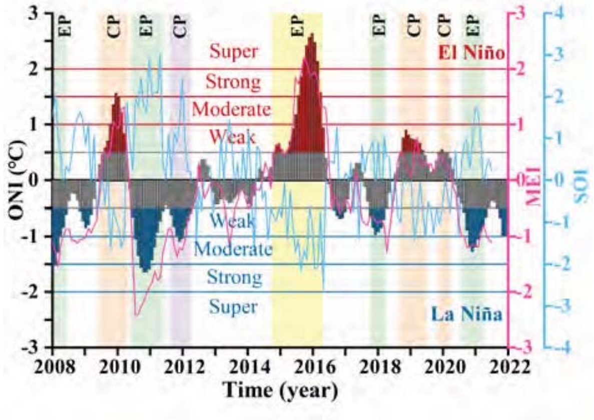

Fig. 3. Time series of ENSO event discriminant index. When SOI ≤ -0.5 for five consecutive months or more, it is considered an El Niño event. When SOI ≥ 0.5 for five consecutive months or more, it is considered a La Niña event. When ONI/MEI ≥ 0.5 for five consecutive months or more, it is considered an El Niño event. When ONI/MEI ≤ -0.5 for five consecutive months or more, it is considered a La Niña event.

D. Study Area Division

This study analyzed the typical spatial distribution characteristics of GNSS ZTD at 260 CMTEMN sites in mainland China for 11.5 years (2010/1–2021/6) using the empirical orthogonal function (EOF) method. EOF can decompose the original data set into patterns ordered by their temporal variances, i.e., the original field of relevant variables is decomposed into several unrelated spatial functions and temporal coefficients [54]. The EOF method has a significant advantage in that the typical field is determined by the characteristics of the variable field sequence rather than being artificially specified in advance, which can better reflect the basic structure of the field. Moreover, the method has a fast convergence rate and easily concentrates a large amount of data information. The first few modes that pass the significance test in the EOF analysis results contain the main variation information of the original field [55]. The EOF decomposition is performed by first constructing the original data covariance matrix [56].

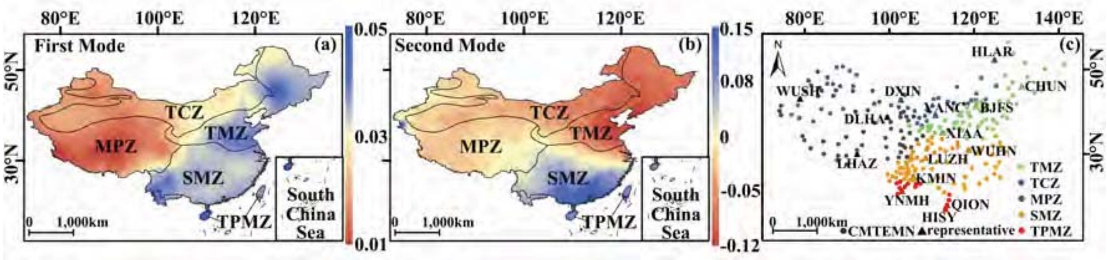

Fig. 4. GNSS ZTD spatial characteristics and regional division results. The red sites belong to the TPMZ, the orange sites belong to the SMZ, the green sites belong to the TMZ, and the blue sites belong to the TCZ, yellow sites belong to MPZ, and the 15 representative sites with special notes (triangles) are the sites shown in the analysis results of this article.

The matrix form of the spatiotemporal grid data is

$$X = \begin{bmatrix} x_{11} & x_{12} & \cdots & x_{1n} \\ x_{21} & x_{22} & \cdots & x_{2n} \\ \vdots & \vdots & \ddots & \vdots \\ x_{m1} & x_{m2} & \cdots & x_{mn} \end{bmatrix} \tag{1}$$

where $X\ (i,\ t)$ is the observation corresponding to position i ($i \in (1,\ m)$) and time t ($t \in (1,\ n)$), m is the spatial station, and n is the time series.

The explanatory rate of the k modality to the total variance can be expressed as

$$\rho_k = \frac{\lambda_k}{\sum_{i=1}^{m} \lambda_i} \times 100\%. \tag{2}$$

The analysis results are tested for significance [57]

$$\Delta\lambda = \lambda\sqrt{\frac{2}{N^*}} \tag{3}$$

where λ represents the characteristic root. A higher λ value indicates that its corresponding modality is more important and contributes more to the total variance. N^* represents the data degrees of freedom. Put λ in rank order and analyze its error range. If the error ranges of the two λ before and after overlap, it does not pass the significance test. The modalities that pass the significance test are the typical characteristics of the original data.

The results show that both the first and second spatial modes passed the significance test [57]. The first mode variance contribution is 87.4%, the second mode variance contribution is 4.04%, and the cumulative contribution of the two modes' variance is 91.44%. The spatial coefficients of the first mode are all positive, reflecting the consistent increase and decrease of GNSS ZTD variation in mainland China, and show a trend of increasing from northwest to southeast [see Fig. 4(a)]. The second modal spatial eigencoefficients are both positive and negative, reflecting the differences in GNSS ZTD variations in different regions [see Fig. 4(b)]. Related studies have shown significant differences in atmospheric humidity and precipitation distributions in different climate regions, and ENSO events have different effects on different climate regions [19], [21], [22]. Therefore, we compared the GNSS ZTD distribution characteristics with the five major climate-type divisions and found that the results were consistent. The first mode shows that the GNSS ZTD in the temperate monsoon zone (TMZ), tropical monsoon zone (TPMZ), and subtropical monsoon zone (SMZ) is higher than in the temperate continental zone (TCZ) and mountain plateau zone (MPZ). The second mode shows the distribution characteristics of GNSS ZTD increases in TMZ and decreases in other regions. The physical mechanism is that the TPMZ and SMZ have high temperatures and rainfall all year round; the TMZ is hot and rainy in summer and cold and dry in winter; the TCZ is far from the ocean and lacks humid air mass transport with low annual rainfall; the MPZ is rainy on the windward side of humid air currents and less precipitation on the leeward side and inside the plateau. There are also related studies showing that the distribution characteristics of GNSS ZTD are associated with the distribution characteristics of meteorological factors such as atmospheric humidity and precipitation [12], [58]. Based on the analysis of this article and the results of related studies, the regional division of the Chinese mainland according to five major climate types is conducted to explore the response patterns of different regional climate changes to ENSO events. The distribution of the partitioned CMTEMN sites is shown in Fig. 4(c).

III. RESPONSE OF GNSS ZTD ANOMALY SEQUENCES TO ENSO EVENTS

A. Selection of Optimum ENSO Index Based on GAMs

The GNSS ZTD anomaly series and MEI time series are complex. They have nonlinear variability, so the linear or nonlinear correlation between GNSS ZTD anomaly and MEI in different regions of mainland China was determined based on generalized additive models (GAMs). GAMs can fit complex nonlinear relationships between the explanatory and response variables into the model [59]. Their core formula is

$$g(u) = f_1(x_1) + f_2(x_2) + \cdots + f_i(x_i) + X_j\theta + \alpha \tag{4}$$

where u represents the expected value of the response variable, $g(u)$ represents the linkage function, $x_1, x_2, \ldots, x_i$ represents the explanatory variable, and $f_i(x_i)$ is a smoothing function of the linear or nonlinear relationship between the explanatory and response variables.

The model does not require the analyst to prespecify the form of the nonlinear relationship. Its use of a smoothing spline function to establish the link between the explanatory and response variables enables the automatic selection of a suitable segmented polynomial. The GAMs are constructed

TABLE II

GAMs MODEL ANALYSIS OF GNSS ZTD ANOMALY IN EACH REGION AND ENSO INDEX

Regions	Explanatory variables	edf	F	P	Deviance explained(%)	R²
TPMZ	ONI	8.49	120.21	<2e-16 ***	49.11	0.4869
	MEI	8.23	123.59	<2e-16 ***	50.5	0.501
	SOI	8.56	50.39	<2e-16 ***	44.71	0.4426
SMZ	ONI	8.87	560.79	<2e-16 ***	46.43	0.4635
	MEI	8.9	824.8	<2e-16 ***	54.6	0.545
	SOI	8.89	490.87	<2e-16 ***	43.21	0.4313
TMZ	ONI	8.72	546.41	<2e-16 ***	47.97	0.4787
	MEI	8.96	615.4	<2e-16 ***	52	0.519
	SOI	8.87	468.69	<2e-16 ***	43.92	0.4382
TCZ	ONI	8.86	440.72	<2e-16 ***	51.6	0.514
	MEI	8.93	1508.3	<2e-16 ***	48.63	0.4854
	SOI	8.9	360.17	<2e-16 ***	45.63	0.4549
MPZ	ONI	8.43	325.87	<2e-16 ***	43.43	0.4331
	MEI	8.54	378.43	<2e-16 ***	43.89	0.4376
	SOI	8.66	230.78	<2e-16 ***	41.48	0.4135

with monthly MEI as the explanatory variable and GNSS ZTD anomaly of the longest time series of each station as the response variables. The degree of correlation between the explanatory and response variables was analyzed. The results of the five regional analyses are shown in Table II. The equivalent degree of freedom (edf) is the number of variables that are not restricted in their values when calculating a statistic. When edf $= 1$, it represents a linear correlation; when edf > 1, it indicates a nonlinear correlation. F represents the set of test statistics, and a larger F value indicates the greater relative importance of the influencing factor. P represents the significance test index, and a smaller P value indicates a more significant correlation. ***indicates that the variable is significant at the 0.001 level. The adjusted coefficient of determination (R^2) is the ratio of the regression sum of squares to the sum of squares of the total deviation. The higher the R^2 and the deviance explained rate, the better the model fitting effect and the stronger the correlation. The effect of each ENSO index on the GNSS ZTD anomaly sequence is demonstrated for the TPMZ (see Fig. 5). The analysis results showed that the three ENSO event indices passed the 0.001 level significance test (they had a significant effect on the variation of GNSS ZTD anomaly in each region at the $P < 0.001$ level). It indicates that the ENSO events were statistically significant as explanatory variables for the variation of GNSS ZTD anomaly. MEI was nonlinearly correlated with GNSS ZTD in each region (edf > 1). The GAM of MEI-GNSS ZTD anomaly in each region has the highest variance explained and R^2, indicating that MEI correlates well with GNSS ZTD anomaly in each region. MEI will be involved in the following analysis as the best ENSO event discriminant index.

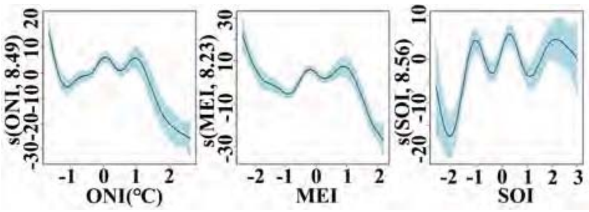

Fig. 5. Effect of the ENSO index on GNSS ZTD anomaly in the TPMZ. The horizontal axis is the explanatory variable, and the vertical coordinate in parentheses is edf. The black line is the fit curve between the explanatory variable and the GNSS ZTD anomaly series. The blue shading is the 95% confidence interval.

B. MEI Threshold for GNSS ZTD Anomaly Response to ENSO Events

Quantifying the correlation between MEI and GNSS ZTD anomaly series is beneficial for the more effective analysis of the influence pattern of ENSO events on climate change in different regions of mainland China. Since the GNSS ZTD anomaly is nonlinearly correlated with MEI, this study chooses to use moving the window correlation analysis (MWCA) to find the correlation coefficient between them. First, the moving window size is determined, and by moving selected windows in the data set analysis, independent local correlation coefficients can be calculated for each window. Thus, a smooth time series of correlation coefficients can be generated [25]. We use the best common period between GNSS ZTD anomaly and MEI as the moving window to reduce their temporal heterogeneity. The significant variation periods of MEI and GNSS ZTD anomaly were extracted by the FFT method. FFT can reflect the amplitude and phase of a time series in the frequency domain [60]. The core equation is

$$x(k) = \frac{1}{N}\sum_{j=1}^{N} X(j) W_N^{(j-1)(k-1)} \tag{5}$$

$$W_N = e^{-j\frac{2\pi}{N}} \tag{6}$$

where $x(k), k = 1, 2, \ldots, N$ denotes the signal characteristics in the frequency domain, $X(j), j = 1, 2, \ldots, N$ denotes the signal characteristics in the time domain.

The analysis results show no significant difference in the significant variation period of GNSS ZTD anomaly sequences among the stations. In this article, four uniformly distributed

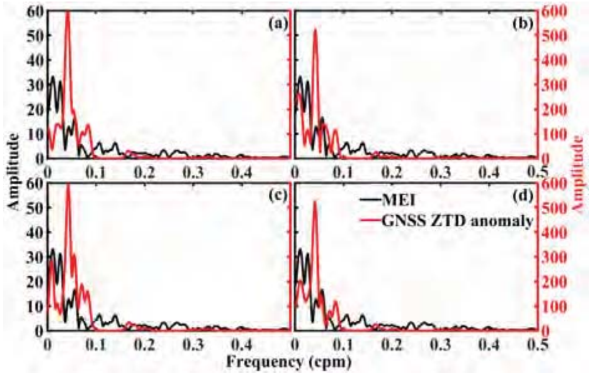

Fig. 6. Common significant variation period between monthly MEI and GNSS ZTD anomaly sequences. (a) BJFS. (b) KMIN. (c) WUHN. (d) WUSH.

TABLE III

CORRELATION COEFFICIENTS OF GNSS ZTD ANOMALY AND ENSO INDEX IN DIFFERENT MOVING WINDOWS

Regions	90 months	40 months	24 months	18 months
TPMZ	0.234	0.332	0.463	0.577
SMZ	0.258	0.353	0.467	0.569
TMZ	0.266	0.356	0.452	0.559
TCZ	0.209	0.340	0.435	0.556
MPZ	0.234	0.349	0.451	0.556

sites were selected to show the analysis results of the common period (see Fig. 6). There are significant 90-month (corresponding to frequency 0.011 cpm), 40-month (0.025 cpm), 24-month (0.042 cpm), and 18-month (0.056 cpm) significant variation cycles of MEI. The GNSS ZTD anomaly sequence also has the same variation period, the most significant of which is the 24-month variation period. The MWCA between GNSS ZTD anomaly and MEI for each station is carried out with four common periods as sliding windows. The comparison results of the mean of the absolute correlation coefficients between GNSS ZTD anomaly and MEI for each region under different moving windows are shown in Table III. The correlation coefficients in Table III all pass the 0.01 level significance test. The results show that the correlations of the regions under the 18-month moving window are better than those under other windows. Therefore, 18 months is the best common period. This analysis is consistent with the views put forward by [25]. The results of sliding correlation analysis between GNSS ZTD anomaly series and MEI in each region are shown in Fig. 7 (randomly selected uniformly distributed stations). Different types of ENSO events have different effects on the GNSS ZTD anomaly in various regions of mainland China. The EP-El Niño event positively affects the GNSS ZTD anomaly in the TPM and SMZ. In the TMZ, TCZ, and MPZ, the GNSS ZTD anomaly has reciprocal responses to the development and decline years of the EP-El Niño event. The EP-El Niño event development year has a negative effect on GNSS ZTD anomaly in the TMZ, TCZ, and MPZ. In contrast, the EP-El Niño recession year positively affects them. The presumed reason is that in the development year of the EP-El Niño event, the East Asian summer monsoon weakened, and the central monsoon rain belt in summer shifted southward. It leads to sufficient PWV in the southern region and is prone to high temperatures and drought in the northern region. In the decay year of the EP-El Niño event, the Western Pacific subtropical high (WPSH) is more potent and located southward. The westward shift of the WPSH transports PWV from the Pacific Ocean to the southern and central-eastern regions of China. The "East Asia-Pacific teleconnection" facilitates the PWV continuous transport from the Arctic Ocean to Northwest China and North China. Therefore, the GNSS ZTD in China is constantly rising during this period [61], [62], [63]. The CP-El Niño event has a negative effect on the GNSS ZTD anomaly of the TMZ, TCZ, TPMZ, and MPZ. It has a positive impact on the SMZ. The reason for this result is the northward position of the WPSH during the CP-El Niño event, and a large amount of Pacific evaporative PWV is transported to the SMZ [64], [65], [66]. Both EP-La Niña and CP-La Niña events positively affect the GNSS ZTD anomaly in mainland China. The presumed reason is that during the La Niña event, the SST in the equatorial eastern Pacific decreased, and the current sea temperature in the western Pacific increased, resulting in a northward shift of the WPSH. It leads to abundant PWV in

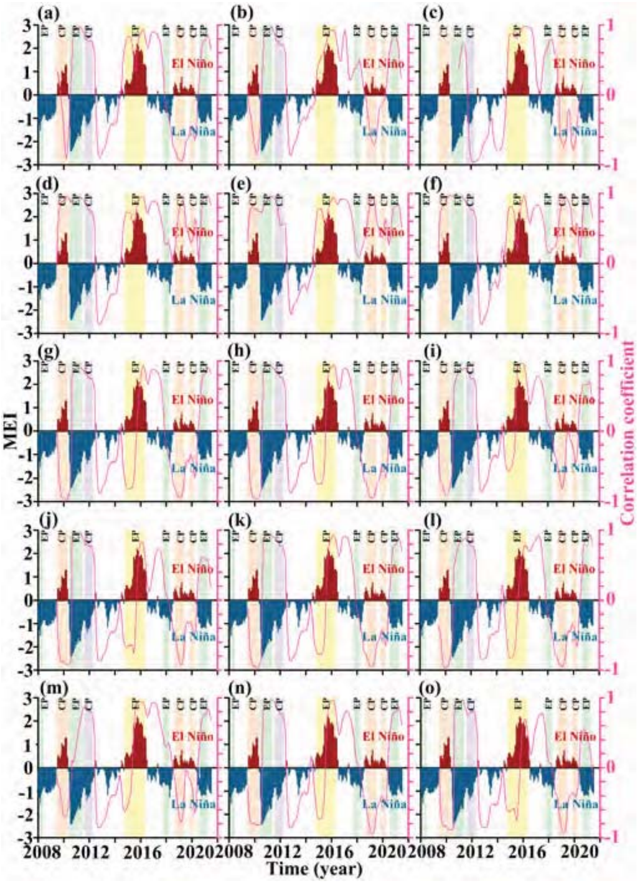

Fig. 7. MWCA of GNSS ZTD anomaly with MEI in each region. (a) HISY_TPMZ. (b) QION_TPMZ. (c) YNMH_TPMZ. (d) KMIN_SMZ. (e) LUZH_SMZ. (f) WUHN_SMZ. (g) CHUN_TMZ. (h) BJFS_TMZ. (i) XIAA_TMZ. (j) YANC_TCZ. (k) DXIN_TCZ. (l) HLAR_TCZ. (m) WUSH_MPZ. (n) DLHA_MPZ. (o) LHAZ_MPZ.

the TMZ, TCZ, and MPZ. Because of the intensely cold air masses from Siberia Mongolia rapidly moving to the southern regions, PWV is continuously transported to Southern China. The meeting of cold and warm air currents increases rain and snow in central China [1], [67]. The PWV and rain/snow content are closely related to GNSS ZTD.

In this study, a linear fit of the correlation between MEI and GNSS ZTD anomaly series was used to quantify the influence of ENSO on GNSS ZTD anomaly in different regions of mainland China and to explore the MEI threshold for GNSS ZTD anomaly response to ENSO events. The correlation coefficients between MEI and GNSS ZTD anomaly series were divided using the percentile method for quantitative analysis. The percentile method is a simple method commonly used to represent the distribution status of variables. The calculation process mainly involves sorting the sample data from smallest to largest, calculating the corresponding cumulative percentile, and then calling the value corresponding to a certain percentile the percentile of that percentile [25]. The total sample size is divided into three parts, with the upper and lower percentiles being 75% and 25%, respectively. The middle 50% is used as the normal part. From the analysis results, it is clear that different regions have different response thresholds to ENSO events (see Fig. 8). The MEI thresholds for GNSS ZTD anomaly in the TPMZ response to El Niño and La Niña events are −1.12 and 1.92, respectively. Therefore, when the MEI exceeds (−1.12, 1.92), the anomalous variation of GNSS ZTD in the TPMZ of China is influenced by ENSO events. Similarly, the MEI thresholds for GNSS ZTD anomaly response to ENSO events are (−1.12, 1.61) for the SMZ, (−1.19, 1.62) for the TMZ, (−1.26, 1.64) for the TCZ, and (−1.22, 1.72) for the MPZ.

IV. Response of GNSS ZTD Oscillation Characteristics to ENSO Events

This study investigates the response of GNSS ZTD frequency-domain oscillation characteristics to ENSO events. The amplitudes of the significant periods in GNSS ZTD for each time frame were compared by intercepting the time frames of different ENSO events from the complete time series and the corresponding normal climate periods. The frequency of variation [cycles per month (cpm)] of each element is analyzed using the FFT with the Hanning window, and the change period (frequency) and amplitude are accurately extracted using the [pks, locs] function. We selected three normal climate periods and one ENSO event period for comparison and analysis to ensure the accuracy and reliability of the results. Based on the completeness of GNSS ZTD data and the duration of ENSO events, six ENSO events that occurred after 2010 were selected for the study (Table IV).

Taking El Niño events as an example, three El Niño events are included in the study period, among which one EP-El Niño event occurred from 2014/10 to 2016/4. We selected three normal climate periods and one EP-El Niño event period for comparison and analysis. The duration of this El Niño event is too long, lasting 19 months, and only one normal climate time series in the studied time series range corresponds to it exactly (2012/10–2014/4). We intercepted 12 months (2015/5–2016/4) forward and backward from the peak time of this event to carry out the analysis to ensure that more experimental groups were compared with it. The significant variation cycles of GNSS ZTD during the four time periods were analyzed using FFT to explore their differences and patterns during the EP-El Niño event compared with normal climate periods. Because of the interception duration of 12 months, the FFT results only showed GNSS ZTD significant periods of nine months (corresponding to a frequency of 0.11) and less, and significant periods within 0.8–3 months [corresponding to a frequency interval of (0.3, 1.3)]. Fig. 9 shows the analysis results of three homogeneously distributed sites from each region.

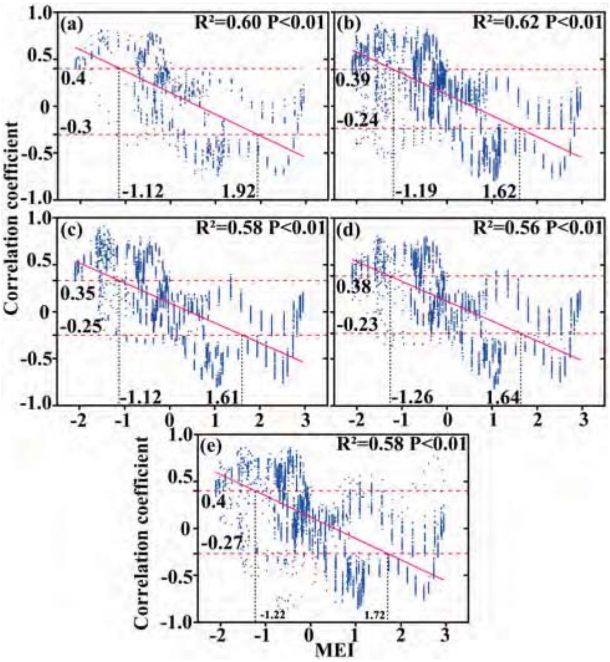

Fig. 8. MEI threshold for GNSS ZTD anomaly in each region response to ENSO events. The pink line is the linear fit between MEI and correlation coefficients of GNSS ZTD anomaly with MEI. (a) TPMZ. (b) SMZ. (c) TMZ. (d) TCZ. (e) MPZ.

TABLE IV
SCREENING OF ENSO EVENTS AND NORMAL CLIMATE COMPARISON PERIOD

ENSO events	Analysis Period	Normal climate1	Normal climate2	Normal climate3
EP-El Niño	2015/5–2016/4	2012/5–2013/4	2013/5–2014/4	2016/5–2017/4
CP-El Niño1	2018/9–2019/6	2012/9–2013/6	2013/9–2014/6	2016/9–2017/6
CP-El Niño2	2019/11–2020/3	2012/11–2013/3	2013/11–2014/3	2016/11–2017/3
EP-La Niña1	2010/6–2011/5	2012/6–2013/5	2013/6–2014/5	2016/6–2017/5
EP-La Niña2	2020/8–2021/3	2012/8–2013/3	2013/8–2014/3	2016/8–2017/3
CP-La Niña	2011/8–2012/3	2012/8–2013/3	2013/8–2014/3	2016/8–2017/3

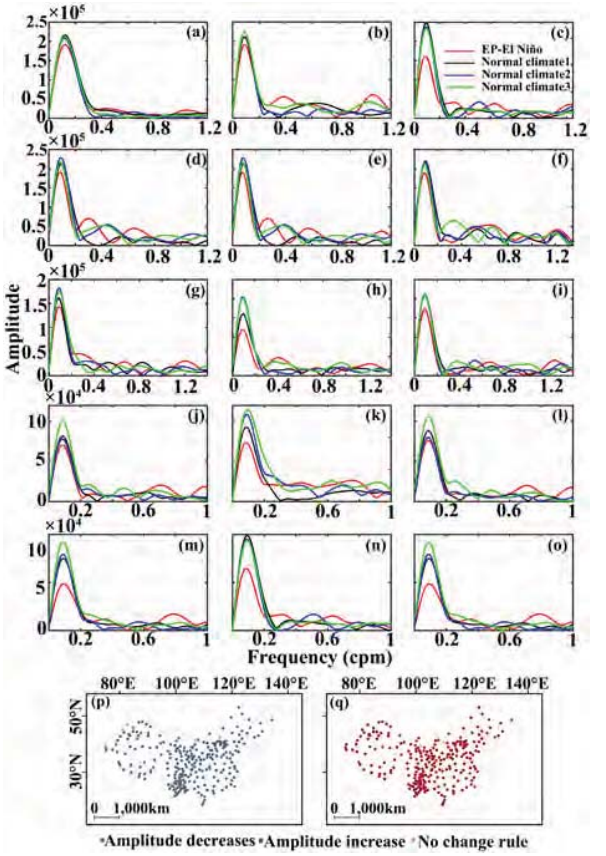

Fig. 9. Response pattern of GNSS ZTD significant change period amplitude to EP-El Niño. (a) HISY_TPMZ. (b) QION_TPMZ. (c) YNMH_TPMZ. (d) KMIN_SMZ. (e) LUZH_SMZ. (f) WUHN_SMZ. (g) CHUN_TMZ. (h) BJFS_TMZ. (i) XIAA_TMZ. (j) YANC_TCZ. (k) DXIN_TCZ. (l) HLAR_TCZ. (m) WUSH_MPZ. (n) DLHA_MPZ. (o) LHAZ_MPZ. Variation of (p) nine-month period and (q) 0.8–3 months period.

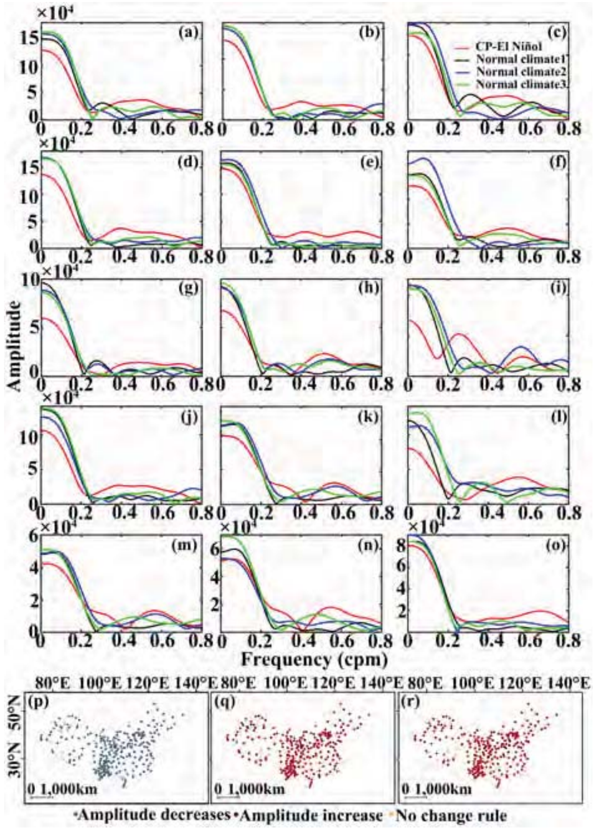

Fig. 10. Response pattern of GNSS ZTD significant change period amplitude to CP-El Niño. (a) HISY_TPMZ. (b) QION_TPMZ. (c) YNMH_TPMZ. (d) KMIN_SMZ. (e) LUZH_SMZ. (f) WUHN_SMZ. (g) CHUN_TMZ. (h) BJFS_TMZ. (i) XIAA_TMZ. (j) YANC_TCZ. (k) DXIN_TCZ. (l) HLAR_TCZ. (m) WUSH_MPZ. (n) DLHA_MPZ. (o) LHAZ_MPZ. Variation of (p) nine-month period, (q) 0.8–3 months period, and (r) 1.2–1.5 months period.

Fig. 9(a)–(c) shows that the amplitude of the nine-month significant variation cycle of GNSS ZTD in the TPMZ during the occurrence of EP-El Niño decreases to different degrees compared with the three normal climate periods. The 2.5- and 0.9-month variation period amplitudes of GNSS ZTD at HISY and QION sites have increased to different degrees, and the 3- and 1.5-month significant variation period amplitudes of GNSS ZTD at the YNMH site have increased significantly. Other regional sites [see Fig. 9(d)–(o)] are analyzed in the same way. The analysis results of each station can be integrated [see Fig. 9(p) and (q)]. Under the influence of the EP-El Niño event, the amplitude of the nine-month significant change cycle of GNSS ZTD in mainland China has different degrees of decrease. In contrast, the amplitude of the 0.8-, 1.2-, 1.5-, and 3-month significant change cycles have different degrees of increase, and only individual stations have no change pattern. These stations are located at higher latitudes in mainland China, with small GNSS ZTD and inactive variations. The northerly wind flow in the northern region is suppressed during this EP-El Niño event, which affects the normal flow of PWV in some regions [68].

Taking the CP-El Niño1 example, the analysis results of three evenly distributed stations were selected from the five climatic type regions for display [see Fig. 10(a)–(o)]. The duration of the CP-El Niño1 is ten months, and the FFT results can only show the GNSS ZTD significant variation period of 1.2–3 months [corresponding to the frequency interval of (0.3, 0.8)] and the linear trend of the partial nine-month significant variation period [see Fig. 10(p) and (q)]. The duration of the CP-El Niño2 is five months, and the FFT results only show the GNSS ZTD significant variation period of 1.2–1.5 months [corresponding to the frequency interval of (0.6, 0.8)] [see Fig. 10(r)]. Under the influence of the CP-El Niño event, the amplitude of the nine-month significant variation period of GNSS ZTD decreases for most stations in mainland China. In contrast, the amplitude of the 1.2–3-month significant variation period increases to different degrees, and only some stations have no variation pattern, which is mainly concentrated in the MPZ.

The effects of La Niña events on the GNSS ZTD significant change period were analyzed using the above analysis method. The aggregated results are shown in Fig. 11. Under the influence of the EP-La Niña event, the amplitude of the nine-month significant variation period of GNSS ZTD decreases at most stations in mainland China [see Fig. 11(a), (c), and (e)], and the amplitude of the significant variation period

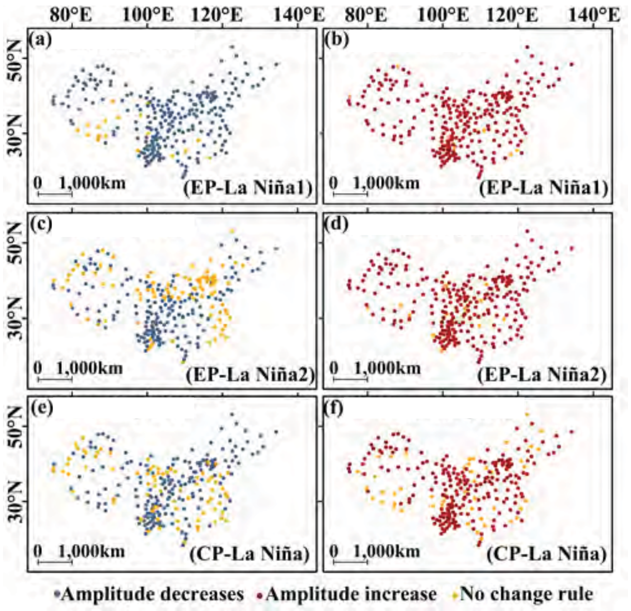

Fig. 11. Response pattern of GNSS ZTD significant change period amplitude to La Niña. (a), (c), and (e) Nine-month period. (b) and (d) One to three months period. (f) 1.2–3 months period.

within one to three months increases to different degrees [see Fig. 11(b), (d), and (f)], while there is no variation pattern at individual stations in the SMZ and the MPZ. The MPZ is far from the origin of ENSO events, and the base of PWV in the SMZ is large and active, so the amplitude of GNSS ZTD significant variation cycle at individual stations shows no variation pattern. The EP-La Niña2 lasts for a shorter time frame. It has a weaker impact on the nine-month significant cycle in China, so the number of stations showing no variation pattern is high. Still, the stations with variation patterns all show a decrease in amplitude.

In summary, the occurrence of ENSO events has an impact on the GNSS ZTD significant variation period in mainland China, which will lead to a decrease in the amplitude of the GNSS ZTD nine-month significant period and an increase in the amplitude of the significant period within 0.8–3 months. Among the four types of ENSO events, the EP-El Niño event has the strongest influence on the significant variation period of GNSS ZTD in China and the most significant regional pattern. In contrast, the CP-La Niña event has the weakest influence on the significant variation period of GNSS ZTD in China and the poor regional pattern.

V. ENSO EVENTS PREDICTION MODELS BASED ON FFT-LSTME

LSTM can fully use long time series data, effectively solving the problem of gradient explosion and disappearance [69]. It introduces the cell state to store long temporal information and can erase, store or write a cell state by controlling three gates (see Fig. 12). The forget gate f_t determines the retention value of the previous cell state c_{t-1}. It consists of the current moment hidden state h_{t-1} and the current moment input data x_t stitched together and passed to the previous moment memory cell. The activation function σ before f_t determines the forgetting gate output value. The input gate i_t determines the retention value of new information. The output gate o_t determines how much information in the memory cell needs to be stored in the hidden state. $\tilde{c}_t$ is a candidate for updating the value. c_t is the memory unit of the current moment, which consists of the previous moment's memory unit multiplied by the forgetting gate to discard part of the information, plus the current moment's content to be updated. c_t becomes a candidate for the output of the hidden layer after the activation function (tanh). The calculation formula is as follows:

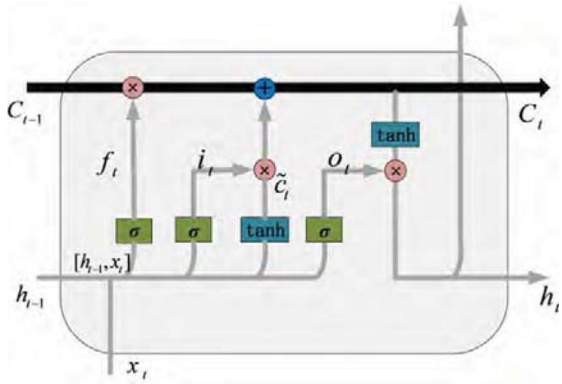

Fig. 12. Structures of LSTM.

$$f_t = \sigma(W_f[h_{t-1}, x_t] + b_f) \tag{7}$$

$$i_t = \sigma(W_i[h_{t-1}, x_t] + b_i) \tag{8}$$

$$\tilde{c}_t = \tanh(W_c[h_{t-1}, x_t] + b_c) \tag{9}$$

$$c_t = f_t c_{t-1} + i_t \tilde{c}_t \tag{10}$$

$$o_t = \sigma(W_o[h_{t-1}, x_t] + b_o) \tag{11}$$

$$h_t = o_t \tanh(c_t). \tag{12}$$

Previous studies have validated the good performance of LSTM models in ENSO event prediction [36], [37], [38], [39], [40]; however, the previous models have the following drawbacks. Most LSTM prediction models are univariate and mainly use the Nino3.4 index or SOI as predictors, and the prediction time horizon is generally 6–12 months. The prediction accuracy and timeliness of ENSO events need to be improved. Aiming at the above problems, a better discriminant index MEI for ENSO events is chosen for prediction. In this study, an FFT-LSTME neural network prediction model integrated with GNSS ZTD was proposed to achieve the prediction of ENSO events for the next 12–24 months. Fig. 13 shows the internal structure of the FFT-LSTME model. The model mainly consists of five subunits, the input data preparation unit [see Fig. 13(a)], the FFT unit [see Fig. 13(b)] for extracting the best common period of each variable, the time-sliding block setting unit [see Fig. 13(c)], the unit of dividing the training set and testing set [see Fig. 13(d)], and the LSTME unit [see Fig. 13(e)] for multisource data fusion and prediction. The workflow of the FFT-LSTME model is as follows: 1) First, the auxiliary input elements of the model are preprocessed. The analysis results in Sections III and IV show that the ENSO event affects the GNSS ZTD anomaly

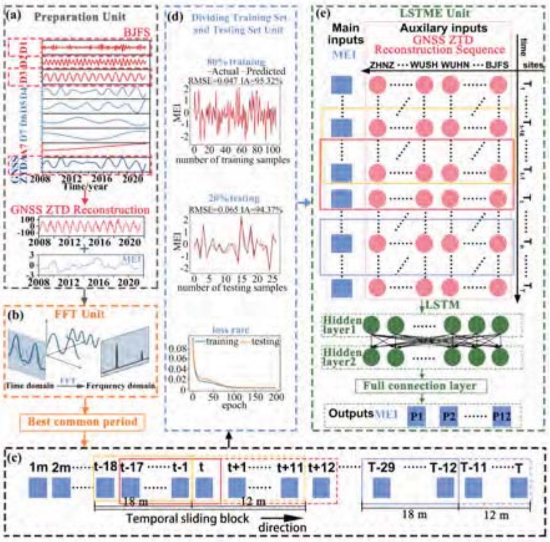

Fig. 13. Construction details of the FFT-LSTME model. (a) Gray dashed box is the data preparation unit to extract the time–frequency feature terms (D1/D3/GNSS ZTDA) of the GNSS ZTD response to the presence of ENSO events using wavelet variation and reconstruct them. (b) Orange dashed box is the FFT unit, which is used to extract the best common period between the GNSS ZTD reconstruction terms and MEI and to provide a reference for the sliding block setting of the model. (c) Black dashed box is the time-sliding window setting unit, where *T* denotes the total duration and *t* denotes the current moment. The yellow, pink, and blue solid boxes indicate the input duration of each slider, and the dashed boxes indicate the output duration of each slider. (d) Blue dashed box is the resulting plot of the division of the training and testing sets. (e) Green dashed box is the LSTME model unit, where the blue squares indicate MEI, the pink dots indicate GNSS ZTD reconstruction sequences for each station in mainland China, and P1, P2, . . . , P12 indicate predicted MEI.

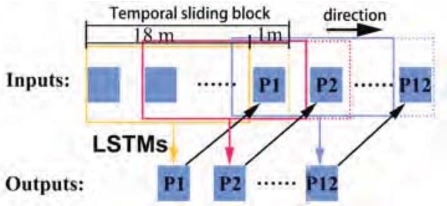

Fig. 14. Temporal sliding block of the FFT-LSTM model. The solid box indicates the input duration, and the dashed box indicates the output duration.

sequence and the nine-month and 0.8–3-month significant variation period of GNSS ZTD. We reconstructed the GNSS ZTD anomaly sequence, the D1 high-frequency term of the GNSS ZTD containing significant periods of 0.8–3 months, and the D3 high-frequency term of the GNSS ZTD containing a significant period of nine months (Fig. 13(a) shows the GNSS ZTD reconstructed sequence) for the BJFS site. Since the GNSS ZTD reconstruction sequence for mainland China responds significantly to the occurrence of ENSO events, it is used as an auxiliary input to the prediction model to add constraints and improve the prediction effectiveness. 2) The GNSS ZTD reconstruction sequences of each station and the MEI sequences of the same period are input into the FFT unit [see Fig. 13(b)]. The FFT can extract the frequency domain variation characteristics of the time series. We use FFT to extract the best common period of MEI and auxiliary elements as the input duration of the model to avoid the impact of temporal heterogeneity between different elements on the prediction accuracy. 3) We put up a temporal sliding block for the prediction model to achieve long-term forecasts [see Fig. 13(c)]. The optimal common period (18 months) of each element derived from step (2) is used as the input duration of each slider. Our previous study proposed an FFT-LSTM model with a temporal sliding block of size (input duration + 1) set up inside (see Fig. 14). If the FFT-LSTM model is applied to predict the ENSO event, the length of the temporal sliding block is 19 months, and the total time series T will be divided into (T-18) groups. Taking the 12-month prediction timeliness as an example, the FFT-LSTM model predicts the MEI of the coming month each time. The predicted value of each experiment is put back into the time series, then trained again, and so on 12 times. The model, however, has two significant drawbacks. One is that putting the predicted values back into the original time series each time will gradually superimpose the prediction error and affect the final prediction accuracy. Another drawback is that the cycle training (T-18) group data will increase the model training time. Therefore, the FFT-LSTME model proposed in this article adjusts the temporal sliding block size to be (input duration + prediction duration). Taking the 12-month prediction timeliness as an example, the time-sliding block size of the FFT-LSTME model is 30 months, and it divides the T into a total of (T-29) groups. We adjust the other hyperparameters of the FFT-LSTME structure to ensure predictive efficacy. 4) The training and testing sets are randomly divided, where 80% of the groups are used for model training and 20% for model testing. The training and testing results of the model are shown for the 12-month prediction time model as an example [see Fig. 13(d)]. The best prediction results were obtained when the loss rate was reduced to 0.01 and below. 5) The FFT-LSTME model connects the auxiliary data and MEI into a unified LSTM input feature vector to provide additional constrained features for ENSO prediction model learning. We set two hidden layers for the LSTM, integrated the main and auxiliary outputs into the fully connected layer, and used the fully connected layer to fuse the features of each element [see Fig. 13(e)]. Finally, the prediction output is generated using the fully connected layer. Normalize all the data before inputting them into the FFT-LSTME model to avoid the impact of the different magnitudes of each feature value and the target value on the prediction performance and to speed up the gradient descent at the same time. Before outputting the predicted value, denormalize the data. After several experiments, the hyperparameters of the FFT-LSTME model are set as follows to achieve the best prediction effect: the iterations parameter (epochs) is 200, the batch_size is 40, and the hidden layer neurons are 48 (under 12-month prediction timeliness). Three metrics were used as accuracy indicators to evaluate the prediction performance of the FFT-LSTME model: RMSE; mean absolute error (MAE); and index of agreement (IA).

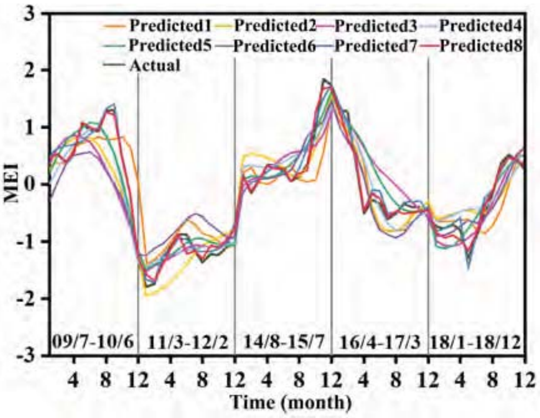

Fig. 15. Comparison of prediction accuracy of FFT-LSTME models with different auxiliary inputs.

These indicators can be expressed as follows:

$$\text{RMSE} = \sqrt{\frac{1}{N}\sum\nolimits_{i=1}^{N}(O_i - P_i)^2} \tag{13}$$

$$\text{MAE} = \frac{1}{N}\sum_{i=1}^{N}|O_i - P_i| \tag{14}$$

$$\text{IA} = 1 - \frac{\sum_{i=1}^{N}(O_i - P_i)^2}{\sum_{i=1}^{N}(|O_i - \overline{O}| + |P_i - \overline{O}|)^2} \tag{15}$$

where N represents the sample number. O_i and P_i are the actual value of MEI and predicted MEI, respectively. $\bar{O}$ is the average MEI. The more minor the RMSE, the smaller the discrepancy between the predicted and actual values. MAE represents the mean of the absolute error between the predicted and actual values. Compared to the RMSE, MAE is absolute and has no positive or negative phase offset. IA indicates the degree of similarity between the predicted and actual values.

VI. DISCUSSIONS

A. Applicability Analysis of GNSS ZTD Reconstruction Sequences Participation in Modeling

Different regions of mainland China respond differently to ENSO events. The TPMZ and SMZ are the closest regions to the Pacific Ocean in mainland China, have abundant PWV, and are significantly affected by ENSO events [19]. The results of Section IV analysis show no response pattern of GNSS ZTD significant variation period to ENSO events at some stations. In order to forecast ENSO events with high quality, the applicability of GNSS ZTD reconstruction sequences for each region to the prediction model needs to be analyzed. The model without any auxiliary input is used as the control group. A total of seven experimental groups were constructed using the GNSS ZTD reconstruction series of the five major climate-type zones, TPM and SMZ, and the entire mainland China, respectively, as auxiliary input variables (see Fig. 15). Each model predicted five sets of MEI of 12-month length. The prediction periods include 2009/7–2010/6, 2011/3–2012/2, 2014/8–2015/7, 2016/4–2017/3, and 2018/1–2018/12. We compare the predicted values with the actual values to evaluate the prediction accuracy of each model, and the evaluation results are shown in Table V. The test results show that the prediction accuracy of the models with the auxiliary data is better than the univariate model. When the Chinese mainland's GNSS ZTD reconstruction sequence is used as the model auxiliary input, the highest prediction accuracy is achieved, with an RMSE of 0.216, an MAE of 0.160, and the IA can reach 95.88%. The different ENSO events cause various degrees of impact on each region of mainland China. The FFT-LSTME model can effectively analyze the nonlinear correlation between the GNSS ZTD reconstruction sequences of different stations and MEI, which plays a good constraint role in the MEI prediction process. Therefore, the auxiliary input of the FFT-LSTME model is the GNSS ZTD reconstruction sequences of each station in mainland China.

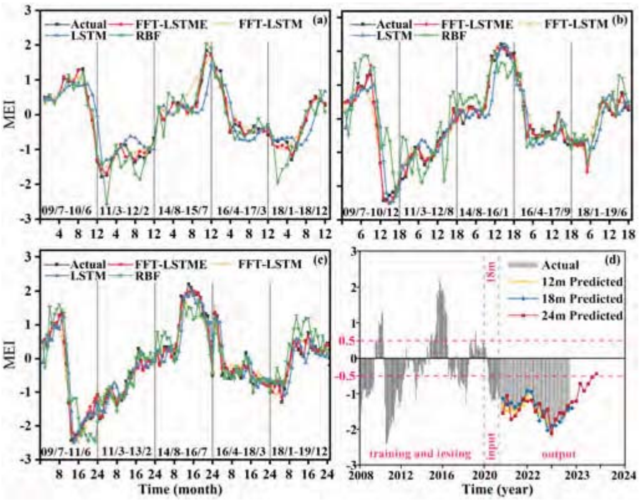

Fig. 16. Evaluation of prediction accuracy of ANNs for ENSO events. (a)–(c) Comparison results of MEI predicted by the four models. (d) Prediction results of the FFT-LSTME model for future ENSO events. (a) 12-month, (b) 18-month, and (c) 24-month predictive timeliness. (d) Predict future ENSO using FFT-LSTME.

B. FFT-LSTME Model Accuracy Evaluation

We chose the RBF, the traditional LSTM model, and our previously proposed FFT-LSTM model [42] to test the prediction performance of the FFT-LSTME model. This study compared the prediction accuracy of the four models at 12, 18, and 24-month prediction timescales and constructed a total of 12 models [see Fig. 16(a)–(c)].

1) The RBF is a feedforward neural network suitable for nonlinear signal processing that can approximate any nonlinear function with arbitrary accuracy and has good local stability and fast convergence of the learning process [70]. Its operational structure consists of an input layer, an output layer, and a hidden layer. Its learning algorithm still needs further improvement. In this study, a Gaussian function with good smoothness and local response characteristics was chosen as the basic function of the hidden layer in the RBF model [71]. The purpose of introducing this model is to verify the superior performance of the LSTM model in ENSO event prediction.

TABLE V

COMPARISON OF PREDICTION ACCURACY OF GNSS ZTD RECONSTRUCTION SEQUENCES IN DIFFERENT REGIONS PARTICIPATING IN MODELING

Predicted value	Region of GNSS ZTD reconstruction sequence	RMSE	MAE
Predicted 1	None	0.383	0.283
Predicted 2	TMZ	0.310	0.265
Predicted 3	TCZ	0.312	0.258
Predicted 4	MPZ	0.316	0.258
Predicted 5	SMZ	0.254	0.223
Predicted 6	TPMZ	0.243	0.206
Predicted 7	TPMZ+SMZ	0.239	0.188
Predicted 8	Mainland China	0.216	0.160

TABLE VI

PREDICTION EFFICIENCY EVALUATION OF DIFFERENT PREDICTION MODELS

Time	Model	RMSE	MAE	IA (%)
12 months	RBF	0.618	0.511	85.39
	LSTM	0.383	0.283	90.98
	FFT-LSTM	0.253	0.196	92.75
	FFT-LSTME	0.216	0.160	95.88
18 months	RBF	0.720	0.646	83.96
	LSTM	0.403	0.295	89.36
	FFT-LSTM	0.262	0.202	90.53
	FFT-LSTME	0.238	0.179	93.37
24 months	RBF	0.847	0.713	80.82
	LSTM	0.446	0.322	87.14
	FFT-LSTM	0.279	0.235	88.57
	FFT-LSTME	0.250	0.183	91.56

2) The traditional LSTM model is suitable for predicting nonlinear time series, but it can only capture the autocorrelation in time and ignores the influence of external factors.

3) Our previously proposed FFT-LSTM model considers external factors' influence, but the temporal sliding block method needs to be refined.

4) The FFT-LSTME model proposed in this study reconstructs the time–frequency feature terms of the GNSS ZTD response to the ENSO events as the auxiliary input to the prediction model. The auxiliary input can constrain the MEI prediction values and improve the prediction accuracy. The temporal sliding block is constructed inside the model to increase the forecast timeliness of the model.

The RBF and LSTM models do not add auxiliary inputs among the four models, and the other two consider auxiliary inputs. The temporal sliding block size is set to (input duration + 1 month) [42] for the FFT-LSTM model and (input duration + prediction duration) for the other three models. The hyperparameters, such as the neurons in the hidden layer, the number of iterations (epochs), batch size, and the ratio of the training set to the test set division, are set consistently for the four models. Five prediction periods were randomly selected from the complete time series. Each of the four models predicted five sets of MEI. The predicted values were compared with the actual values to evaluate the prediction accuracy. The evaluation results of each model are shown in Table VI. The results of the comparison experiments show that the FFT-LSTME model can predict ENSO events in the next 24 months with an IA of 91.56% and an RMSE of 0.25. The RMSE is optimized by 70.48%, 43.95%, and 11.6% when compared with RBF, LSTM, and FFT-LSTM. The IA of FFT-LSTME reaches more than 90% under 12–24 months prediction timeliness.

In addition, we used the FFT-LSTME model to predict future ENSO events [see Fig. 16(d)]. Because of the limited length of the acquired GNSS ZTD event series (2008/1–2021/6), the available data were divided into two major parts. The MEI and GNSS ZTD from January 2008 to December 2019 as the model training part, and the training set (80%) and the testing set (20%) were randomly divided. The data set from January 2020 to June 2021 (18 months) as model inputs. The MEI for the next 12, 18, and 24 months are predicted. Currently, the MEI is updated to November 2022, and the model's predicted values match well with the known values for 17 months. From the prediction results, it can be concluded that global climate changes will continue to be affected by La Niña events since July 2021, and this La Niña event is expected to end in May or June 2023. According to the above analysis results, the La Niña event increases the PWV in mainland China. Strong cold air currents from the south and warm air from the north collide, increasing the rain and snow in north-central China. The relevant meteorological departments should do a good job of early warning and advance prevention to reduce or prevent the impact and loss caused by extreme weather on people's health and social development.

C. Contributions and Limitations

This study analyzed the nonlinear correlation characteristics between three ENSO discriminant indices and GNSS ZTD anomaly using GAMs and screened out the best ENSO discriminant index MEI. We explored the response patterns of GNSS ZTD to different ENSO events in each region of mainland China from the time domain and frequency domain, respectively. An ENSO event prediction model incorporating GNSS ZTD is constructed based on FFT-LSTME. The main contributions of the study are as follows. 1) We determined that MEI is the most significant ENSO event discriminant index associated with the GNSS ZTD in mainland China through experiments and analysis. 2) The response patterns of GNSS ZTD time–frequency variations to ENSO events in different climate-type regions of mainland China were investigated and obtained. 3) An ENSO event prediction model (FFT-LSTME) is established by incorporating GNSS ZTD based on LSTM. The best common variation period of MEI and GNSS ZTD is extracted using FFT. It is used to determine the input duration of the model to decrease the effect of temporal heterogeneity among variables on the model's prediction accuracy. Monitoring and predicting ENSO events using GNSS ZTD is a new prospective method. 4) A time-sliding block is established inside the FFT-LSTME model to make the model can obtain the long-term variation pattern of time series and achieve longer timeliness and higher accuracy prediction. It can provide references for relevant meteorological monitoring and disaster prevention and control management departments. The limitations of this study and the outlook for future work are as follows. 1) ENSO events are interannual variability events. The most extended time series of high-precision GNSS ZTD provided by the CMTEMN is 14.5 years, which has some limitations. ENSO events impact global climate changes, and the analysis of the response pattern of GNSS ZTD to ENSO events in China alone cannot be applied to other countries and regions. In the future, we will accumulate more experimental data and research the correlation between GNSS ZTD and ENSO events on a global scale over a more extended period. 2) This study aims to verify the feasibility of using GNSS ZTD to improve the prediction accuracy of ENSO events and only introduces GNSS ZTD as an auxiliary variable. ENSO events affect the changes of multiple meteorological elements globally. The previous prediction approaches also lacked the consideration of multiple external influences. In the future, we will integrate multiple meteorological factors such as solar activity, drought and flood indicators, and temperature to build ENSO event prediction models and further improve their accuracy. We will also try integrating the discriminant indices of different distribution types of ENSO events (EP-ENSO index and CP-ENSO index) into the prediction model to accurately predict different distribution types of ENSO events.

VII. CONCLUSION

In response to the existing quantitative analysis of ENSO event effects on the climate change in mainland China is insufficient, we introduce GNSS ZTD into ENSO event monitoring and quantify the response pattern of GNSS ZTD time–frequency variation to ENSO events. From the three common ENSO discriminant indices, such as MEI, ONI, and SOI, we selected the MEI with the most significant correlation characteristics with GNSS ZTD for the study. It is concluded that the MEI thresholds for the existence of response to ENSO events are different for different climate-type regions zones in mainland China. The MEI thresholds for GNSS ZTD anomaly response to ENSO events are (−1.12, 1.92) for the TPMZ, (−1.12, 1.61) for the SMZ, and (−1.19, 1.62) for the TMZ. The TCZ is (−1.26, 1.64); the MPZ is (−1.22, 1.72). The ENSO event has an impact on the significant variation period of GNSS ZTD in mainland China, which will lead to a decrease in the amplitude of the nine-month significant variation period of GNSS ZTD and an increase in the amplitude of the significant variation period within 0.8–3 months.

Aiming at the problems of the prediction accuracy and timeliness of ENSO events are still low, and the FFT-LSTME prediction model was constructed. This model applies the GNSS ZTD reconstruction sequence of mainland China as an auxiliary input variable, reduces the influence of temporal heterogeneity of different variables by using FFT, and enhances the prediction timeliness using its internal time-sliding block. Compared with the existing models, the FFT-LSTME effectively improves the prediction accuracy and achieves longer prediction. The RMSE of MEI prediction values for the next 12, 18, and 24 months are 0.216, 0.238, and 0.250, respectively, and the IA are 95.88%, 93.37%, and 91.56%, respectively. The RMSE of the FFT-LSTME model was optimized by 70.48%, 43.95%, and 11.6% over RBF, LSTM, and FFT-LSTM, respectively, at a 24-month prediction timescale. This study verified the feasibility of using GNSS ZTD as an auxiliary variable to improve the prediction efficiency of ENSO events and provided a new ENSO event prediction method. The model can help relevant meteorological departments to predict extreme weather more accurately.

ENSO events are interannual variability events with global impact. There are some limitations in this article's study duration and area. In the future, we will accumulate more experimental data, expand the scope of the study, and consider more meteorological factors such as solar activity, drought and flood indicators, and temperature to build ENSO event prediction models to improve their accuracy further. We will also try integrating the discriminant indices of different distribution types of ENSO events (EP-ENSO index and CP-ENSO index) into the prediction model to accurately predict different distribution types of ENSO events.

ACKNOWLEDGMENT

The authors would like to thank the First Monitoring and Application Center, China Earthquake Administration for providing China Mainland Tectonic Environment Monitoring Network (CMTEMN) zenith tropospheric delays (ZTDs), National Climate Center of China Meteorological Administration for providing the El Niño-Southern Oscillation (ENSO) event statistics yearbook (http://cmdp.ncc-cma.net/pred/cn_enso_index.php), and National Oceanic and Atmospheric Administration (NOAA) for providing multivariate ENSO index (MEI), Southern Oscillation index (SOI), and Oceanic Niño index (ONI) (https://psl.noaa.gov/enso/).

REFERENCES

[1] C. Shi et al., "Analysis of '21.7' extreme rainstorm process in Henan Province using BeiDou/GNSS observation," *Chin. J. Geophys.*, vol. 65, no. 1, pp. 186–196, 2022.

[2] W. Chen, S. Ding, J. Feng, S. Chen, X. Xue, and Q. Zhou, "Progress in the study of impacts of different types of ENSO on the east Asian monsoon and their mechanisms," *Chin. J. Atmos. Sci.*, vol. 42, no. 3, pp. 640–655, 2018.

[3] Y. Wang and Y. Liu, *Theory and Application of Ground-based GPS Meteorology*. Beijing, China: Surveying and Mapping Press, 2012, pp. 1–42.

[4] M. Wu, S. Jin, Z. Li, Y. Cao, F. Ping, and X. Tang, "High-precision GNSS PWV and its variation characteristics in China based on individual station meteorological data," *Remote Sens.*, vol. 13, no. 7, p. 1296, Mar. 2021, doi: 10.3390/rs13071296.

[5] R. Li et al., "Advances in BeiDou navigation satellite system (BDS) and satellite navigation augmentation technologies," *Satell. Navigat.*, vol. 1, no. 1, p. 12, Mar. 2020, doi: 10.1186/s43020-020-00010-2.

[6] M. Bevis, S. Businger, T. A. Herring, C. Rocken, R. A. Anthes, and R. H. Ware, "GPS meteorology: Remote sensing of atmospheric water vapor using the global positioning system," *J. Geophys. Res.*, vol. 97, no. D14, Oct. 1992, Art. no. 15787, doi: 10.1029/92JD01517.

[7] S. Jin, Q. Wang, and G. Dardanelli, "A review on multi-GNSS for Earth observation and emerging applications," *Remote Sens.*, vol. 14, no. 16, p. 3930, Aug. 2022, doi: 10.3390/rs14163930.

[8] T. Hadas, T. Hobiger, and P. Hordyniec, "Considering different recent advancements in GNSS on real-time zenith troposphere estimates," *GPS Solut.*, vol. 24, no. 4, p. 99, Jul. 2020, doi: 10.1007/s10291-020-01014-w.

[9] S. Jin, L. Han, and J. Cho, "Lower atmospheric anomalies following the 2008 Wenchuan earthquake observed by GPS measurements," *J. Atmos. Solar-Terr. Phys.*, vol. 73, nos. 7–8, pp. 810–814, May 2011, doi: 10.1016/j.jastp.2011.01.023.

[10] B. Zhou, X. Li, Y. Chen, and M. Zeng, "Effect of the GPS ZTD data assimilation on simulation of typhoon 'Lekima,'" *J. Meteorol. Sci.*, vol. 40, no. 1, pp. 11–21, 2020.

[11] Y. Q. Z. Yao Zhao Li and Y. He, "Short-term precipitation forecasting based on the data from GNSS observation," *Adv. Water Sci.*, vol. 27, no. 3, pp. 357–365, 2016, doi: 10.14042/j.cnki.32.1309.2016.03.003.

[12] Y. Wang, Z. Lou, Y. Liu, and Z. Hao, "ZTD long time series characteristics of IGS stations in China and their relationship with annual precipitation," *J. Geod. Geodyn.*, vol. 39, no. 10, pp. 1037–1040, 2019, doi: 10.14075/j.jgg.2019.10.010.

[13] Y. Yao, Y. Luo, J. Zhang, and C. Zhao, "Correlation analysis between haze and GNSS tropospheric delay based on coherent wavelet," *Geomat. Inf. Sci. Wuhan Univ.*, vol. 43, no. 12, pp. 2131–2138, 2018, doi: 10.13203/j.whugis20180234.

[14] Q. Zhao, Y. Ma, Z. Li, and Y. Yao, "Retrieval of a high-precision drought monitoring index by using GNSS-derived ZTD and temperature," *IEEE J. Sel. Topics Appl. Earth Observ. Remote Sens.*, vol. 14, pp. 8730–8743, 2021, doi: 10.1109/JSTARS.2021.3106703.

[15] C. Giannaros, V. Kotroni, K. Lagouvardos, T. M. Giannaros, and C. Pikridas, "Assessing the impact of GNSS ZTD data assimilation into the WRF modeling system during high-impact rainfall events over Greece," *Remote Sens.*, vol. 12, no. 3, p. 383, Jan. 2020, doi: 10.3390/rs12030383.

[16] M. Guo, H. Zhang, and P. Xia, "Analysis of short-time weather forecast based on GNSS zenith troposphere delay," *Sci. Surv. Mappin*, vol. 46, no. 4, pp. 28–36, 2021, doi: 10.16251/j.cnki.1009-2307.2021.04.005.

[17] Q. Zhao, Y. Liu, X. Ma, W. Yao, Y. Yao, and X. Li, "An improved rainfall forecasting model based on GNSS observations," *IEEE Trans. Geosci. Remote Sens.*, vol. 58, no. 7, pp. 4891–4900, Jul. 2020, doi: 10.1109/TGRS.2020.2968124.

[18] H. Li et al., "A new cumulative anomaly-based model for the detection of heavy precipitation using GNSS-derived tropospheric products," *IEEE Trans. Geosci. Remote Sens.*, vol. 60, pp. 1–18, 2022, Art. no. 4105718, doi: 10.1109/TGRS.2021.3137014.

[19] F. Ren, Y. Yuan, C. Sun, and L. Cao, "Review of progress of ENSO studies in the past three decades," *Adv. Meteorol. Sci. Technol.*, vol. 2, no. 3, pp. 17–24, 2012.

[20] H.-Y. Kao and J.-Y. Yu, "Contrasting eastern-pacific and central-pacific types of ENSO," *J. Climate*, vol. 22, no. 3, pp. 615–632, Feb. 2009, doi: 10.1175/2008JCLI2309.1.

[21] L. Cao, C. Sun, F. Ren, Y. Yuan, and J. Jiang, "Study of a comprehensive monitoring index for two types of ENSO events," *J. Trop. Meteorol.*, vol. 29, no. 1, pp. 66–74, 2013.

[22] J. Lei and C. Huang, "Temperature, precipitation and response to ENSO in different regions of China in the past 30 years," *Trop. Geomorphol.*, vol. 39, no. 2, pp. 12–19, 2018.

[23] J. Foster et al., "El Niño, water vapor, and the global positioning system," *Geophys. Res. Lett.*, vol. 27, no. 17, pp. 2697–2700, Sep. 2000, doi: 10.1029/2000GL011429.

[24] S. Barindelli, E. Realini, G. Venuti, A. Fermi, and A. Gatti, "Detection of water vapor time variations associated with heavy rain in northern Italy by geodetic and low-cost GNSS receivers," *Earth, Planets Space*, vol. 70, no. 1, p. 28, Feb. 2018, doi: 10.1186/s40623-018-0795-7.

[25] Q. Zhao, Y. Liu, W. Yao, X. Ma, and Y. Yao, "A novel ENSO monitoring method using precipitable water vapor and temperature in southeast China," *Remote Sens.*, vol. 12, no. 4, p. 649, Feb. 2020, doi: 10.3390/rs12040649.

[26] Y.-B. Yao, C-Y. He, B. Zhang, and C.-Q. Xu, "A new global zenith tropospheric delay model GZTD," *Chin. J. Geophys.*, vol. 56, no. 7, pp. 2218–2227, Jul. 2013.

[27] Y. Wang, T. Yu, X. Liu, and W. Zhan, "GNSS ZTD time series in Beijing-Tianjin-Hebei region and their response to El Niño events," *J. Nanjing Univ. Inf. Sci. Technol.*, vol. 13, no. 2, pp. 170–180, 2021, doi: 10.13878/j.cnki.jnuist.2021.02.006.

[28] X. Fang and R. Xie, "A brief review of ENSO theories and prediction," *Sci. China Earth Sci.*, vol. 63, no. 4, pp. 476–491, Apr. 2020, doi: 10.1007/s11430-019-9539-0.

[29] H.-L. Ren et al., "A review of research on tropical air-sea interaction, ENSO dynamics, and ENSO prediction in China," *J. Meteorolog. Res.*, vol. 34, no. 1, pp. 43–62, Feb. 2020, doi: 10.1007/s13351-020-9155-1.

[30] M. Pal, R. Maity, J. V. Ratnam, M. Nonaka, and S. K. Behera, "Long-lead prediction of ENSO modoki index using machine learning algorithms," *Sci. Rep.*, vol. 10, no. 1, p. 365, Jan. 2020, doi: 10.1038/s41598-019-57183-3.

[31] Y.-G. Ham, J.-H. Kim, and J.-J. Luo, "Deep learning for multi-year ENSO forecasts," *Nature*, vol. 573, no. 7775, pp. 568–572, Sep. 2019, doi: 10.1038/s41586-019-1559-7.

[32] D. He, J. Jiang, H. Hao, and P. Lin, "Research on ENSO forecasting method based on deep learning," *Frontiers Data Comput.*, vol. 10, no. 1, pp. 38–47, 2019.

[33] M. Aslam, J.-M. Lee, H.-S. Kim, S.-J. Lee, and S. Hong, "Deep learning models for long-term solar radiation forecasting considering microgrid installation: A comparative study," *Energies*, vol. 13, no. 1, p. 147, Dec. 2019, doi: 10.3390/en13010147.

[34] W. Mao, W. Wang, L. Jiao, S. Zhao, and A. Liu, "Modeling air quality prediction using a deep learning approach: Method optimization and evaluation," *Sustain. Cities Soc.*, vol. 65, Feb. 2021, Art. no. 102567, doi: 10.1016/j.scs.2020.102567.

[35] M. Thangavelu, V. J. Parthiban, D. Kesavaraman, and T. Murugesan, "Forecasting of solar radiation for a cleaner environment using robust machine learning techniques," *Environ. Sci. Pollut. Res.*, vol. 30, pp. 30919–30932, Nov. 2022, doi: 10.1007/s11356-022-24321-w.

[36] A. Huang, B. Vega-Westhoff, and R. L. Sriver, "Analyzing El Niño–Southern Oscillation predictability using long-short-term-memory models," *Earth Space Sci.*, vol. 6, no. 2, pp. 212–221, Feb. 2019, doi: 10.1029/2018EA000423.

[37] F. Chen, "The prediction of ENSO indexes based on time series LSTM model," *Climate Change Res. Lett.*, vol. 8, no. 3, pp. 287–295, 2019, doi: 10.12677/CCRL.2019.83032.

[38] P. Zhou, Y. Huang, B. Hu, and J. Wei, "Spring predictability barrier phenomenon in ENSO prediction model based on LSTM deep learning algorithm," *Acta Sci. Nat. Univ. Pekin.*, vol. 57, no. 6, pp. 1071–1078, 2021, doi: 10.13209/j.0479-8023.2021.114.

[39] Y. Guo, X. Cao, B. Liu, and K. Peng, "El Niño index prediction using deep learning with ensemble empirical mode decomposition," *Symmetry*, vol. 12, no. 6, p. 893, Jun. 2020, doi: 10.3390/sym12060893.

[40] M. Gupta, H. Kodamana, and S. Sandeep, "Prediction of ENSO beyond spring predictability barrier using deep convolutional LSTM networks," *IEEE Geosci. Remote Sens. Lett.*, vol. 19, pp. 1–5, 2022, doi: 10.1109/LGRS.2020.3032353.

[41] X. Li et al., "Long short-term memory neural network for air pollutant concentration predictions: Method development and evaluation," *Environ. Pollut.*, vol. 231, pp. 997–1004, Dec. 2017, doi: 10.1016/j.envpol.2017.08.114.

[42] T. Yu, Y. Wang, J. Huang, X. Liu, J. Li, and W. Zhan, "Study on the regional prediction model of PM2.5 concentrations based on multi-source observations," *Atmos. Pollut. Res.*, vol. 13, no. 4, Apr. 2022, Art. no. 101363, doi: 10.1016/j.apr.2022.101363.

[43] J. Chen, S. Yang, W. Tan, J. Wang, and Y. Zhang, "Recent results of the Chinese CMONOC GNSS network," in *Proc. ION Pacific PNT Meeting*, Honolulu, HI, USA, May 2017, pp. 539–546, doi: 10.33012/2017.15077.

[44] S. Wu et al., "Analysis of deterministic and stochastic models of GPS stations in the crustal movement observation network of China," *Adv. Space Res.*, vol. 64, no. 2, pp. 335–351, Jul. 2019.

[45] H. Shi, R. Zhang, Z. Nie, Y. Li, Z. Chen, and T. Wang, "Research on variety characteristics of mainland China troposphere based on CMONOC," *Geodesy Geodynamics*, vol. 9, no. 5, pp. 411–417, Sep. 2018, doi: 10.1016/j.geog.2018.06.007.

[46] L. Li, Y. Song, and J. Zhou, "Preliminary exploration of GNSS meteorological elements using wavelet transform for rainstorm prediction," *J. Geod. Geodyn.*, vol. 40, no. 3, pp. 225–230, 2020, doi: 10.14075/j.jgg.2020.03.002.

[47] Y. Tian, J. Gao, and D. Wang, "Synchrosqueezing optimal basic wavelet transform and its application on sedimentary cycle division," *IEEE Trans. Geosci. Remote Sens.*, vol. 60, 2022, Art. no. 5908413, doi: 10.1109/TGRS.2021.3127268.

[48] F. Cai, F. Sun, H. Dai, X. Zhu, and L. Zhang, "Application of wavelet and Fourier transform in time series analysis," *GNSS World China*, vol. 44, no. 4, pp. 40–46, 2019, doi: 10.13442/j.gnss.1008-9268.2019.04.006.

[49] S. He, G. Li, H. Liu, and L. Dong, "Application and research of optimal wavelet base selection method in seismic data processing," *South China J. Seismol.*, vol. 39, no. 3, pp. 49–56, 2019, doi: 10.13512/j.hndz.2019.03.007.

[50] J. L. McBride and N. Nicholls, “Seasonal relationships between Australian rainfall and the southern oscillation,” *Monthly Weather Rev.*, vol. 111, no. 10, pp. 1998–2004, Oct. 1983.

[51] K. E. Trenberth, “The definition of El Niño,” *Bull. Am. Meteorol. Soc.*, vol. 78, no. 12, pp. 2771–2778, Dec. 1997, doi: 10.1175/1520-0477(1997)078<2771: TDOENO>2.0.CO.2.

[52] K. Wolter and M. S. Timlin, “Measuring the strength of ENSO events: How does 1997/98 rank?” *Weather*, vol. 53, no. 9, pp. 315–324, 1998, doi: 10.1002/j.1477-8696.1998.tb06408.x.

[53] X. Wang, Q.-Y. Liu, D. Sui, and D. Wang, “The imprint of the ENSO activities on the south China sea wave climate,” *Ocean Dyn.*, vol. 70, no. 10, pp. 1315–1323, Oct. 2020.

[54] A. Hannachi and A. O’Neill, “Atmospheric multiple equilibria and non-Gaussian behaviour in model simulations,” *Quart. J. Roy. Meteorolog. Soc.*, vol. 127, no. 573, pp. 939–958, Apr. 2001, doi: 10.1002/qj.49712757312.

[55] J. Wu, “Sea surface wind speed retrieval based on empirical orthogonal function analysis using 2019–2020 CYGNSS data,” *IEEE Trans. Geosci. Remote Sens.*, vol. 60, 2022, Art. no. 5803213, doi: 10.1109/TGRS.2022.3169832.

[56] A. Hannachi, I. T. Jolliffe, and D. B. Stephenson, “Empirical orthogonal functions and related techniques in atmospheric science: A review,” *Int. J. Climatol.*, vol. 27, no. 9, pp. 1119–1152, Jul. 2007, doi: 10.1002/joc.1499.

[57] G. R. North, T. L. Bell, R. F. Cahalan, and F. J. Moeng, “Sampling errors in the estimation of empirical orthogonal functions,” *Mon. Weather Rev.*, vol. 110, no. 7, pp. 699–706, Jul. 1982, doi: 10.1175/1520-0493(1982)110<0699: SEITEO>2.0.CO.2.

[58] O. A. Isioye, L. Combrinck, and J. Botai, “Evaluation of spatial and temporal characteristics of GNSS-derived ZTD estimates in Nigeria,” *Theor. Appl. Climatol.*, vol. 132, nos. 3–4, pp. 1099–1116, May 2018, doi: 10.1007/s00704-017-2124-7.

[59] T. J. Hastie, “Generalized additive models,” in *Statistical Models in S*. Evanston, IL, USA: Routledge, 1992.

[60] Y. Zheng, “A brief talk on FFT (fast Fourier transform) algorithm and its application,” *Sci. Technol.*, vol. 25, no. 29, p. 144, 2015.

[61] Y. Wu, Y. Ding, and Y. Liu, “A new study of El Niño impacts on summertime water vapor transport and rainfall in China,” *Acta Meteor. Sinica.*, vol. 75, pp. 371–383, Jan. 2017.

[62] P. Zhai, R. Yu, and Y. Guo, “The strong El Niño in 2015/2016 and its dominant impacts on global and China’s climate,” *ActaMeteorolog. Sinica.*, vol. 74, no. 3, pp. 309–321, 2016.

[63] J. Zhou, Z. Zuo, and X. Rong, “Comparison of the effects of soil moisture and El Niño on summer precipitation in eastern China,” *Sci. China Earth Sci.*, vol. 63, no. 2, pp. 267–278, Feb. 2020, doi: 10.1007/s11430-018-9469-6.

[64] M. Chen, T. Li, and X. Wang, “Asymmetry of atmospheric responses to two-type El Niño and La Niña over Northwest Pacific,” *J. Meteorolog. Res.*, vol. 33, no. 5, pp. 826–836, Oct. 2019, doi: 10.1007/s13351-019-9022-0.

[65] K. Liu, J. Chen, and R. Yang, “Connection between two leading modes of autumn rainfall interannual variability in Southeast China and two types of ENSO-like SSTA,” *Adv. Meteorol.*, vol. 2019, pp. 1–14, Aug. 2019, doi: 10.1155/2019/1762505.

[66] Y. Yuan, H. Yang, and C. Li, “Study of El Niño events of different types and their potential impact on the following summer precipitation in China,” *Acta Meteorolog. Sinica.*, vol. 70, no. 3, pp. 467–478, 2012.

[67] W. Zhang, X. Zhou, P.-C. Hsu, and F. Liu, “Diversity of east China summer rainfall change in post-El Niño summers,” *Frontiers Earth Sci.*, vol. 8, Dec. 2020, Art. no. 595548, doi: 10.3389/feart.2020.595548.

[68] M. Liu, H. Ren, W. Zhang, and P. Ren, “Influence of super El Niño events on the frequency of spring and summer extreme precipitation over eastern China,” *Acta Meteorol. Sin.*, vol. 76, no. 4, p. 15, 2018.

[69] X. Cao, Y. Guo, B. Liu, K. Peng, G. Wang, and Gao, “ENSO prediction based on long short-term memory (LSTM),” *IOP Conf. Ser. Mater. Sci. Eng.*, vol. 799, no. 1, 2020, Art. no. 012035, doi: 10.1088/1757-899X/799/1/012035.

[70] J. F. Qiao, H. G. Han, and J. F. Qiao, “Optimal structure design for RBFNN structure,” *Acta Autom. Sinica*, vol. 36, no. 6, pp. 865–872, 2010.

[71] X. Gao, “A nonlinear prediction model for Chinese speech signal based on RBF neural network,” *Multimedia Tools Appl.*, vol. 81, no. 4, pp. 5033–5049, Feb. 2022, doi: 10.1007/s11042-021-11612-6.

Tengli Yu was born in Hebei, China, in 1997. She received the B.S.E. degree from Shijiazhuang Tiedao University, Shijiazhuang, China, in 2019, and the M.Eng. degree from Tianjin Chengjian University, Tianjin, China, in 2022, both in geomatics engineering. She is currently pursuing the Ph.D. degree with Shenyang Aerospace University, Shenyang, China.

Her research interests include the Global Navigation Satellite System (GNSS) meteorology and aircraft navigation and positioning algorithms.

Ershen Wang was born in Liaoning, China, in 1980. He received the Ph.D. degree in communication and information systems from Dalian Maritime University, Dalian, China, in 2009.

From January 2014 to December 2016, he worked as a Postdoctoral with Beihang University, Beijing, China. He is currently a Professor with the School of Electronic and information engineering, Shenyang Aerospace University, Shenyang, China. He is the lead of the Key Laboratory of Navigation and Surveillance technology. He has published over 80 articles in peer-reviewed journals and proceedings, 20 patents/software copyrights. His research interests include BeiDou Navigation Satellite System (BDS) /Global Navigation Satellite System (GNSS) positioning theory and signal processing, integrity monitoring, integrated navigation, target tracking, artificial intelligence, and applications to unmanned systems.

Dr. Wang is a member of Liaoning General Aviation Academy, Shenyang.

Shuanggen Jin (Senior Member, IEEE) was born in Anhui, China, in 1974. He received the B.Sc. degree from Wuhan University, Wuhan, China, in 1999, and the Ph.D. degree from the University of Chinese Academy of Sciences, Beijing, China, in 2003, both in geodesy.

He is currently the Vice-President and Professor with Henan Polytechnic University, Jiaozuo, China, and also a Professor with Shanghai Astronomical Observatory, Chinese Academy of Sciences (CAS), Shanghai, China. He has published over 500 articles in peer-reviewed journals and proceedings, ten patents/software copyrights, and ten books/monographs with more than 10 000 citations and an H-index >52. His main research areas include Satellite Navigation, remote sensing, and space/planetary exploration.

Dr. Jin was an International Association of Geodesy (IAG) Fellow, International Union of Geodesy and Geophysics (IUGG) Fellow, fellow of the Electromagnetics Academy, fellow of the African Academy of Sciences, a World Class Professor of the Ministry of Education and Cultures, Indonesia, a Chief Scientist of the National Key Research and Development Program, China, a member of the Russian Academy of Natural Sciences, the European Academy of Sciences, the Turkish Academy of Sciences, and the Academia Europaea. He received the 100-Talent Program of CAS, Leading Talent of Shanghai. He was the President of the International Association of Planetary Sciences (IAPS) (2015–2019), the President of the International Association of Chinese Professionals in Global Positioning Systems (CPGPS) (2016–2017), the Chair of the IUGG Union Commission on Planetary Sciences (UCPS) (2015–2023), an Editor-in-Chief of *International Journal of Geosciences*, an Editor of *Geoscience Letters*, an Associate Editor of IEEE TRANSACTIONS ON GEOSCIENCE AND REMOTE SENSING and *Journal of Navigation*, and an Editorial Board Member of *Remote Sensing GPS Solutions*, and *Journal of Geodynamics*.

Yong Wang was born in Jiangxi, China, in 1978. He received the B.S.E. and M.Eng. degrees in geomatics engineering from Henan Polytechnic University, Henan, China, in 2000 and 2003, respectively, and the Ph.D. degree in geodesy and survey engineering from the Institute of Surveying and Geophysics, Chinese Academy of Sciences (CAS), Wuhan, China, in 2007.

He is currently a Professor with Tianjin Chengjian University, Tianjin, China. He has published over 70 academic articles and three monographs. His research interests include the Global Navigation Satellite System (GNSS) meteorology and geological hazard monitoring research.

Dr. Wang is an Editorial Board Member of the *Journal of Catastrophology*, a member of the State Key Laboratory of Geodesy and Earth's Dynamics, Innovation Academy for Precision Measurement Science and Technology, CAS, the Steering Committee of Engineering Professional Degree Education, Tianjin, and the Education and Science Working Committee of Tianjin Society of Surveying and Mapping.

Jing Huang was born in Anhui, China, in 1996. He received the B.S.E. degree from Tianjin Chengjian University, Tianjin, China, in 2020, where he is currently pursuing the M.Eng. degree in geomatics engineering.

His research interest is Global Navigation Satellite System (GNSS) application research.

Xiao Liu was born in Shandong, China, in 1997. She received the B.S.E. degree from Shijiazhuang Tiedao University, Shijiazhuang, China, in 2019, and the M.Eng. degree from Tianjin Chengjian University, Tianjin, China, in 2022, both in geomatics engineering.

She is currently working with the First Monitoring and Application Center, China Earthquake Administration, Tianjin. Her research interest is Global Navigation Satellite System (GNSS) application research.

Wei Zhan was born in Jiangxi, China, in 1983. He received the M.Eng. degree from the Institute of Surveying and Geophysics, Chinese Academy of Sciences, Wuhan, China, in 2007, and the Ph.D. degree from Wuhan University, Wuhan, in 2017.

He is currently a Researcher with the First Monitoring and Application Center, China Earthquake Administration, Tianjin, China. He is also a Graduate Student Mentor with Tianjin Chengjian University, Tianjin. His research interests include the Global Navigation Satellite System (GNSS) data fine processing and crustal deformation mechanism research.